Sr 2 MgMoO 6 − δ : Structure, Phase Stability, and Cation Site Order Control of Reduction

5 AUTHORS, INCLUDING:

Carlos Bernuy-López
Norwegian University of Science and Techno…
10 PUBLICATIONS **111** CITATIONS

SEE PROFILE

Craig A Bridges
Oak Ridge National Laboratory
78 PUBLICATIONS **1,113** CITATIONS

SEE PROFILE

John Bleddyn Claridge
University of Liverpool
154 PUBLICATIONS **4,904** CITATIONS

SEE PROFILE

Sr₂MgMoO₆₋δ: Structure, Phase Stability, and Cation Site Order Control of Reduction

Carlos Bernuy-Lopez, Mathieu Allix, Craig A. Bridges, John B. Claridge,* and Matthew J. Rosseinsky*

Department of Chemistry, The University of Liverpool, Liverpool L69 7ZD, United Kingdom

Received October 9, 2006. Revised Manuscript Received December 12, 2006

The potential solid oxide fuel cell anode material Sr_2MgMoO_6 adopts a $\sqrt{2} \times \sqrt{2} \times 2$ $I\bar{1}$ superstructure of the simple perovskite cell, derived from an $a^0a^0c^-$ tilt system via distortion of the Mg- and Mo-centered octahedra. Reduction of Sr_2MgMoO_6 appears to be correlated with antisite disorder at either point or extended antiphase defects. The degree of reduction is small at temperatures below 900 °C. Upon further reduction above 900 °C, Sr_2MgMoO_6 begins to decompose into a reduced material modeled as an $n = 2$ Ruddlesden–Popper phase with a significantly higher Mo:Mg ratio, MgO, and Mo. Diffraction data are consistent with the reduced material being significantly intergrown with the perovskite matrix.

Introduction

Solid-oxide fuel cells are of importance for stationary and distributed power generation at high thermodynamic efficiency, offering opportunities for efficient utilization of both natural gas/hydrocarbons or hydrogen as a fuel. Current active materials chemistry research themes include reducing the cathode overpotential by enhancing oxide catalytic activity for oxygen reduction, identifying oxide ion conductors operating at low temperatures to reduce materials compatibility problems, and identifying mixed-oxide ion conductors with suitable chemical stability to reduction in H_2 or CH_4 at high temperature to function as anodes.[1–4] The double perovskite Sr_2MgMoO_6 has recently been shown to offer excellent performance as a fuel-cell anode,[5,6] combining the required chemical stability, electronic and ionic conductivity, and electrocatalytic activity in the highly reducing atmosphere of the fuel-cell anode with resistance to poisoning by sulfur impurities in the fuel, a severe problem when considering the use of methane in the form of natural gas. The chemical and structural factors controlling the extent to which oxygen can be removed from Sr_2MgMoO_6 are important, as removal of O under reducing conditions is required both for the introduction of anion vacancies to permit ionic conduction and for reduction of $5d^0$ Mo(VI) to $5d^1$ Mo(V) to generate electronic carriers. The original report shows Sr_2MgMoO_6 is a rock-salt B-site-ordered double perovskite with Mo(VI) surrounded by six Mg^{2+} neighbors. In this paper, we report the detailed structural chemistry of this material and the chemical and structural changes that take place on reduction. This reveals the limited extent to which oxygen loss is possible in the pure material and the interplay between structure and chemistry that permit reduction to occur.

Experimental Section

Sr_2MgMoO_6 was prepared by direct reaction of MoO_3, MgO, and $SrCO_3$ at 950 °C for 15 h. The powder was reground, pressed into pellets, and refired at 1250 °C for 44 h, with a second regrinding and pelletizing and firing at 1350 °C for 44 h. Sample II was prepared by reduction in 5% H_2/N_2 at 800 °C for 18 h. Reduction of sample I at 1200 °C for 12 h in a flow of 5% H_2/N_2 gave samples III and IV, which were brown/black in color; IV was prepared on a smaller scale (1 g) than III (5 g) and reduced under rigorously O_2-free H_2. These conditions are similar to those used by Huang et al.[5,6] for the initial preparation of $Sr_2MgMoO_{6-\delta}$.

Structural characterization of the materials was carried out using laboratory PXRD data collected on a PANALYTICAL Xpert system using Co Kα_1 radiation in Bragg Brentano geometry. Time-of-flight (TOF) PND data were collected at ambient temperature on HRPD and POLARIS at ISIS. Data were refined by the Rietveld method[7,8] using the GSAS software package and the EXPGUI interface.[9] In the case of all samples, separate refinements were carried out against PXRD and the highest resolution TOF bank. Because pf the strong pseudo-symmetry, the least-squares refinements were carried out using the Levenberg–Marquardt algorithm rather than the Gauss–Newton algorithm, in order to obtain better convergence. The Stephens approach[10] was applied to the anisotropic peak shapes in all cases. In the X-ray refinements, thermal parameters were fixed at 0.01 Å², as was the oxygen content, but Mg/Mo antisite disorder and a surface absorption correction were refined. In the neutron refinements, Mg/Mo antisite disorder was fixed at the value obtained for the X-ray refinement and the isotropic thermal parameters, and anion vacancy concentrations were refined.

Samples for transmission electron microscopy were prepared by crushing the powder in *n*-butanol, and the small crystallites in

(1) Lashtabeg, A.; Skinner, S. J. *J. Mater. Chem.* **2006,** *16,* 3161–3170.
(2) McIntosh, S.; Gorte, R. J. *Chem. Rev.* **2004,** *104,* 4845–4865.
(3) Zhao, S. P.; Haile, S. M. *Nature* **2004,** *431,* 170–173.
(4) Tao, S.; Irvine, J. T. S. *Nat. Mater.* **2003,** *2,* 320–323.
(5) Huang, Y. H.; Dass, R. I.; Denyszyn, J. C.; Goodenough, J. B. *J. Electrochem. Soc.* **2006,** *153,* A1266–A1272.
(6) Huang, Y. H.; Dass, R. I.; Xing, Z. L.; Goodenough, J. B. *Science* **2006,** *312,* 254–257.
(7) Rietveld, H. M. *Acta Crystallogr.* **1967,** *22,* 151.
(8) Rietveld, H. M.; *J. Appl. Crystallogr.* **1969,** *2,* 65.
(9) Toby, B. H.; *J. Appl. Crystallogr.* **2001,** *34* (2), 210–213.
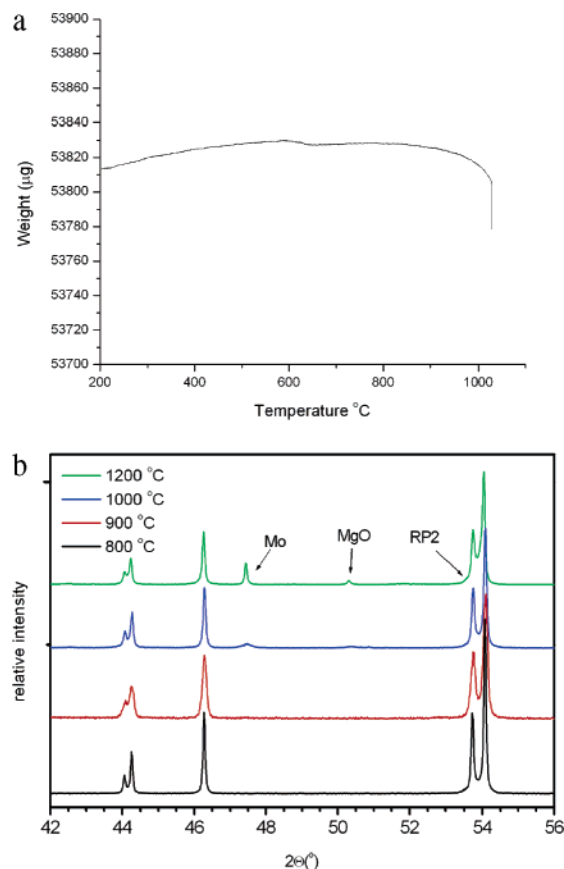(10) Stephens, P. W., *J. Appl. Crystallogr.* **1999,** *32,* 281–289.

Figure 1. (a) Thermogravimetric analysis of the reduction of Sr_2MgMoO_6 in 5% H_2 in N_2. (b) Powder X-ray diffractograms for Sr_2MgMoO_6 reduced for 12 h in flowing 5% H_2/N_2 between 800 and 1200 °C. Peaks attributed to MgO and Mo are marked. The shoulder marked RP2 corresponds to the formation of $n = 2$ Ruddlesden−Popper intergrowths.

Figure 2. Selected area electron diffractograms of the [001] and [010] projections of air-synthesized Sr_2MgMoO_6 (sample I), showing systematic absences consistent with an I-centered cell.

suspension were deposited onto a holey carbon film, supported by a copper grid. The electron diffraction (ED) study was carried out with a JEOL 2000FX electron microscope. Energy dispersive spectroscopy (EDS) analyses were systematically carried out during the ED study, the JEOL 2000FX being equipped with EDAX analyzer. Thermal analysis (TGA) was performed using a Seiko SII-TG/DTA 6300 thermal analyzer.

Results

In the case of sample I of Sr_2MgMoO_6 (air-fired), the powder X-ray diffraction data indicated the formation of a B-site-ordered perovskite plus a trace amount of strontium molybdate ($SrMoO_4$). The sample was greenish white and contained no new phases. Prior to the final anneal, significantly more strontium molybdate and other unidentified impurities were present.

Initial inspection of the PXRD data for sample III (reduced at 1200 °C for 12 h) indicated that a degree of decomposition had occurred (peaks attributed to MgO and Mo were present in the pattern); therefore, reduction at lower temperatures was investigated, initially by TGA measurement in a reducing atmosphere. Figure 1a shows that there was only a very minor weight loss at about 600 °C and a gradual weight loss starting at ~800 °C observed and that the reduction proceeded relatively slowly even up to 1100 °C, with a total of ~0.03 oxygen per Sr_2MgMoO_6 formula unit being lost in 1 h. As shown in Figure 1b, both the samples reduced at

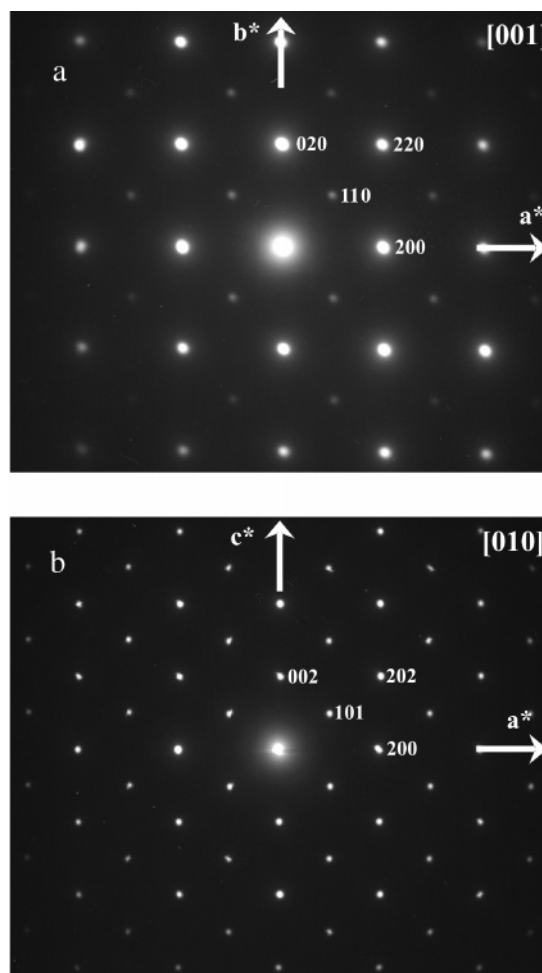800 and 900 °C did not contain any apparent MgO or Mo impurity phases. In light of this observation and the reported reduction of Sr_2MgMoO_6 at 800 °C,[5] a further sample was prepared by reduction in 5% H_2/N_2 at 800 °C for 18 h (Sample II). Sample II was a darker green than the initial sample I but much paler than sample III.

Analysis of sample I (Sr_2MgMoO_6) by EDS in the TEM for sample I confirmed its homogeneity and that the correct cation composition had been maintained in the synthesis. Reconstruction of the reciprocal space of Sr_2MgMoO_6 by electron diffraction revealed a cell of dimensions $\sqrt{2}a_p \times \sqrt{2}a_p \times 2a_p$, with only the body centring $h + k + l = 2n$ reflection condition (Figure 2) being inconsistent with the initially reported space group of $P2_1/n$ (0k0, $k = 2n$; h0l, $h + l = 2n$). The patterns are metrically tetragonal; however, splittings are observed in the X-ray and neutron diffraction data.

Identification of the correct structural description of Sr_2MgMoO_6 required comparative analysis of possible tetragonal, orthorhombic, monoclinic, and triclinic solutions against the high-resolution neutron powder diffraction data. This procedure is challenging because of the very pronounced pseudocubic symmetry. Refinement in I4/mmm, I4/m, and *Immm* ($\chi^2 = 12.2$) were all unsatisfactory. It was possible to converge a satisfactory refinement in I2/m ($\chi^2 = 1.7$), but
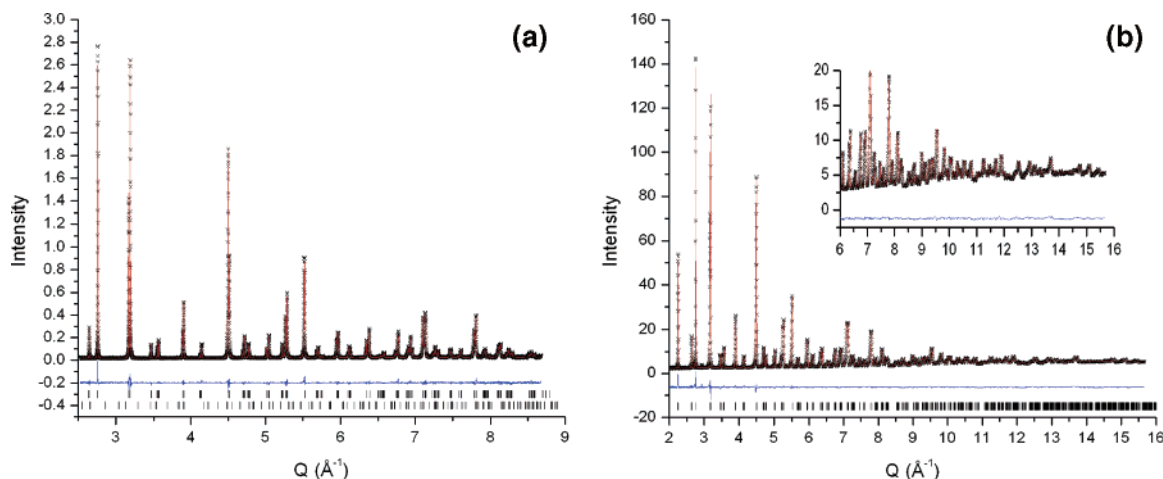
Figure 3. (a) Rietveld refinement of the backscattering bank neutron diffraction data from HRPD of sample I of Sr_2MgMoO_6. Crosses are observed data, the solid red line is the calculated pattern, and the blue line is the difference. The upper set of tick marks corresponds to the positions of the Bragg peaks for Sr_2MgMoO_6, and the lower set the positions of the Bragg peaks of the $SrMoO_4$ impurity. (b) Rietveld refinement of the backscattering bank neutron diffraction data from Polaris of sample II of $Sr_2MgMoO_{6−\delta}$, plotted as in part a above. The tick marks mark the positions of the Bragg peaks for $Sr_2MgMoO_{6−\delta}$. The inset shows the fit at high Q.

Table 1. Refinement Parameters, Refined Cell Constants. and Phase Fractions (quoted in wt %) for the $Sr_2MgMoO_{6\pm\delta}$ Present

	I		II		III	
	X-ray	HRPD	X-ray	Polaris	X-ray	HRPD
χ^2	4.118	1.469	2.878	4.475	5.777	5.088
$R(F^2)$ (%)	4.34	4.55	5.11	4.93	4.30	6.59
a (Å)	5.569321(14)	5.56666(2)	5.56980(2)	5.56903(4)	5.57151(1)	5.57299(3)
b (Å)	5.569448(23)	5.56612(2)	5.56958(2)	5.57042(4)	5.57773(4)	5.57745(4)
c (Å)	7.923445(24)	7.91916(2)	7.92380(2)	7.92406(5)	7.92034(4)	7.92129(5)
α (deg)	89.961(1)	89.991(2)	89.988(1)	89.977(6)	89.892(1)	89.940(1)
β (deg)	89.989(0)	89.972(1)	89.999(2)	90.009(4)	89.923(1)	90.024(1)
γ (deg)	90.013(0)	89.996(2)	90.005(2)	90.0016(3)	89.923(1)	89.953(1)
V (Å^3)	245.770(1)	245.373(1)	245.808(1)	245.819(3)	246.135(2)	246.218(3)
phase fraction $Sr_2MoMgO_{6\pm\delta}$	98.866(1)	98.927(3)	98.027(2)	100	84.56(2)	86.24(3)
phase fraction Mo					1.47(2)	0.89(3)
phase fraction MgO					2.31(7)	1.17(2)
phase fraction $SrMoO_4$	1.13(3)	1.07(3)	1.97(2)			
phase fraction $Sr_3(Mo_{(1−x)}Mg_x)_2O_{7−\delta}$					11.65(9)	11.13(9)

the model was inadequate from a crystal chemical viewpoint: analysis with isotropic displacement parameters in this space group converges only to $\chi^2 = 2.86$, so anisotropic displacement parameters are needed to match the observed intensities. This description produces a large discrepancy in the size and shape of the displacement ellipsoids of the two crystallographically distinct oxide anion sites in the $I2/m$ structural description, with O2 having an equivalent isotropic ellipsoid four times the size of that of O1. This suggested that in $I2/m$, O2 was accounting for more than one distinct anion site in the true structure. Refinements in $I2$ and Im were unsatisfactory, but analysis in $I\bar{1}$ (Figure 3 and Tables 1−3) gave superior agreement ($\chi^2 = 1.47$), as has been previously observed in a number of cases in which the MO_6 octahedra are distorted,[11,12] with only isotropic displacement parameters required at each site. The origin of this improvement is the splitting of the O2 site in $I2/m$ to O2 and O2b in $I\bar{1}$. Attempts to model this instead by splitting the O2 site in $I2/m$ yield less of an improvement than the $I\bar{1}$ model ($\chi^2 = 1.79$ vs 1.47). It is important to note that the unit cell of Sr_2MgMoO_6 is metrically tetragonal (all the angles are 90° within error; $(b − a)/a$ is 1×10^{-4}, whereas $(c − a)/a$ is 0.6

$\times 10^{-2}$), so it is the intensities that decide the appropriateness of a structural model.

The neutron powder diffraction data are relatively insensitive to the antisite disorder of Mg and Mo. The strong differences in X-ray scattering power makes X-ray powder diffraction more suitable for defining the extent to which the strict alternation of Mg and Mo on the B sites is violated and thus a separate refinement against X-ray data was carried out. The results of both refinements are summarized in Tables 1 and 2.

In the case of sample II (800 °C 5% H_2 in N_2), there is again a dominant double perovskite phase; in the PXRD data, weak peaks for $SrMoO_4$ are visible but these are lost in the noise in the TOF neutron data and thus not refined (Figure 3b). For sample III, ((1200 °C 5% H_2 in N_2) the powder X-ray diffraction data indicated the formation of a B-site ordered perovskite plus MgO, Mo, and an unidentified impurity that appears as shoulders on some of the perovskite peaks (Figure 4). These impurity peaks are more prominent in the case of sample IV produced on a smaller scale under more reducing conditions. (see the Supporting Information, Figure S1). Analysis of the sample by EDS in the TEM for samples III and IV confirmed the presence of MgO and the homogeneity of the remaining crystallites indicating that $Sr_2MgMoO_{6−\delta}$, Mo, and the new phase are intimately mixed

(11) Battle, P. D.; Goodenough, J. B.; Price, R. *J. Solid State Chem.* **1983**, *46*, 234−244.
(12) Ohashi, Y.; Finger, L. W. *Am. Mineral.* **1978**, *63*, 274−288.

Table 2. Refined Atomic Parameters for the $Sr_2MgMoO_{6\pm\delta}$ and Phase in Samples I, II, and III (fixed parameters are in italic)[a]

	I		II		III	
	X-ray	HRPD	X-ray	Polaris	X-ray	HRPD
Sr1						
x	0.5026(5)	0.5019(5)	0.4946(3)	0.5023(4)	0.4894(2)	0.4955(4)
y	−0.0020(5)	−0.0009(8)	0.0050(3)	0.0016(3)	0.0025(2)	−0.0122(3)
z	0.2475(6)	0.2486(5)	0.2534(2)	0.2501(5)	0.2470(3)	0.2451(3)
U	0.0066(1)	0.01453(9)	*0.01*	0.00969(4)	*0.01*	0.0116(2)
Mo1						
U	0.0037(1)	0.00565(21)	*0.01*	0.00520(3)	*0.01*	0.0069(3)
F	0.992(1)	*0.992*	0.987(1)	*0.987*	0.933(1)	*0.933*
Mg1						
U	0.0037(1)	0.01635(31)	*0.01*	0.00520(3)	*0.01*	0.0097(4)
F	0.992(1)	*0.992*	0.987(1)	*0.987*	0.933(1)	*0.933*
O1						
x	−0.0274(9)	−0.0119(5)	−0.0266(14)	−0.006(1)	−0.015(2)	0.0006(9)
y	0.0013(10)	0.0065(9)	0.0249(15)	−0.0153(2)	0.009(3)	0.0127(5)
z	0.2414(4)	0.2448(2)	0.2404(3)	0.2470(3)	0.2311(7)	0.2464(5)
U	*0.01*	0.01687(7)	*0.01*	0.01193(7)	*0.01*	0.0143(3)
O2						
x	0.2577(9)	0.2733(3)	0.2854(8))	0.2665(2)	0.225(1)	0.2749(4)
y	0.2090(10)	0.2143(3)	0.2194(9)	0.2263(2)	0.281(2)	0.2207(4)
z	−0.0079(4)	−0.0044(5)	0.0092(18)	−0.0080(2)	0.023(1)	−0.0012(5)
U	*0.01*	0.01687(7)	*0.01*	0.01269(8)	*0.01*	0.0143(3)
O2b						
x	−0.2193(11)	−0.2237(3)	−0.2164(10)	−0.2147(1)	−0.261(1)	−0.2249(4)
y	0.2857(10)	0.2665(4)	0.2443(10)	0.2751(2)	0.220(1)	0.2525(5)
z	−0.0159(13)	0.0078(3)	0.0173(11)	−0.0080(2)	−0.021(1)	−0.011035
U	*0.01*	0.01687(7)	*0.01*	0.00520(3)	*0.01*	0.024(4)
F	*1.0*	*1.0*	*1.0*	0.993(2)	*1.0*	0.977(5)

[a] Mo1 is on 2(a) (0,0,0) and Mg1 on 2(b) (0.5,0.5,0). The refined model has a total octahedral site occupancy of 1.00, with the difference from the refined fraction F quoted here made up by the occupancy of $1 - F$ of Mg on Mo1 and Mo on Mg1.

Table 3. Refined Parameters for the $Sr_3(Mo_{1-x}Mg_x)_2O_{7-\delta}$ Ruddlesden−Popper Impurity Phase in Sample III[a]

atom	x	y	z	occupancy
Sr1	0	0	0.5	1
Sr2	0	0	0.3005(5)	1
Mo1	0	0	0.1058(5)	0.784(12)
O1	0	0	0	0.49(3)
O2	0	0	0.1904(6))	1
O3	0		0.1025(4)	1

[a] Space group $I4/mmm$, $a = 3.9527(2)$ Å, $c = 20.436(5)$ Å, $V = 319.29(8)$ Å^3, overall $U = 0.01(1)$ Å^2, $x = 0.215(9)$, $\delta = 0.49(3)$.

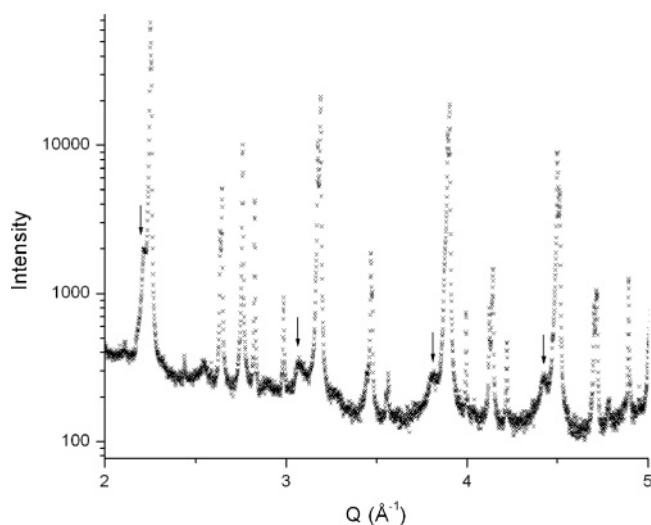**Figure 4.** Powder X-ray diffraction data for sample III of $Sr_2MgMoO_{6-\delta}$ reduced at 1200 °C. The arrows indicate the shoulders on peaks attributed to the $n = 2$ Ruddlesden−Popper phase.

on the EDS length scale (approximately >100 nm). Reconstruction of the reciprocal space of $Sr_2MgMoO_{6-\delta}$ by electron diffraction in the TEM revealed a cell of dimensions $\sqrt{2}a_p$ × $\sqrt{2}a_p$ × $2a_p$ with only the body-centering $h + k + l = 2n$ reflection condition, as for sample I prepared in air. (Figure 5a) In some crystallites, extra reflections were observed as well as streaking and diffuse features along $(001)_{perov}$ (Figure 5b−d). The strongest extra reflections in both neutron and X-ray powder data are characteristic of an $n = 2$ Ruddlesden−Popper phase, and the observed shoulders occur close to the peak positions expected for $Sr_3Mo_2O_7$.[13,14] This is consistent with electron diffraction patterns revealing streaking along c^* in the perovskite (Figure 5b), the coexistence of perovskite and $n = 2$ Ruddlesden−Popper unit cells (Figure 5c), and patterns solely indexable as from the bilayered Ruddlesden−Popper phase with streaking along the layer stacking direction (Figure 5d).

Refinements of the neutron and X-ray diffraction data from sample III that did not include the RP second phase did not give satisfactory fits ($\chi^2 = 8.595$ for the HRPD backscattering bank). Both X-ray and TOF neutron refinements significantly improved on addition of the RP phase ($\chi^2 = 5.088$ for the HRPD backscatter bank) (Figure 6) Refined parameters for the RP phase from analysis of the HRPD data are given in Table 3. An overall thermal parameter was used in both neutron and X-ray refinements; Mo:Mg ratios on the octahedral site were refined in the X-ray data and fixed in the neutron refinement, where the anion occupancies were varied. The RP phase B-site cation composition in the neutron refinement was fixed at the value obtained from the X-ray data, and only the phase fractions were refined as detailed above. The refined cation ratios in the entire multiphase assemblage in sample III can be calculated from

(13) Shirakawa, N.; Ikeda, S. I. *Physica C* **2000**, *341*, 783−784.
(14) Steiner, U.; Reichelt, W. *Z. Naturforsch., B: Chem. Sci.* **1998**, *53*, 110−116.
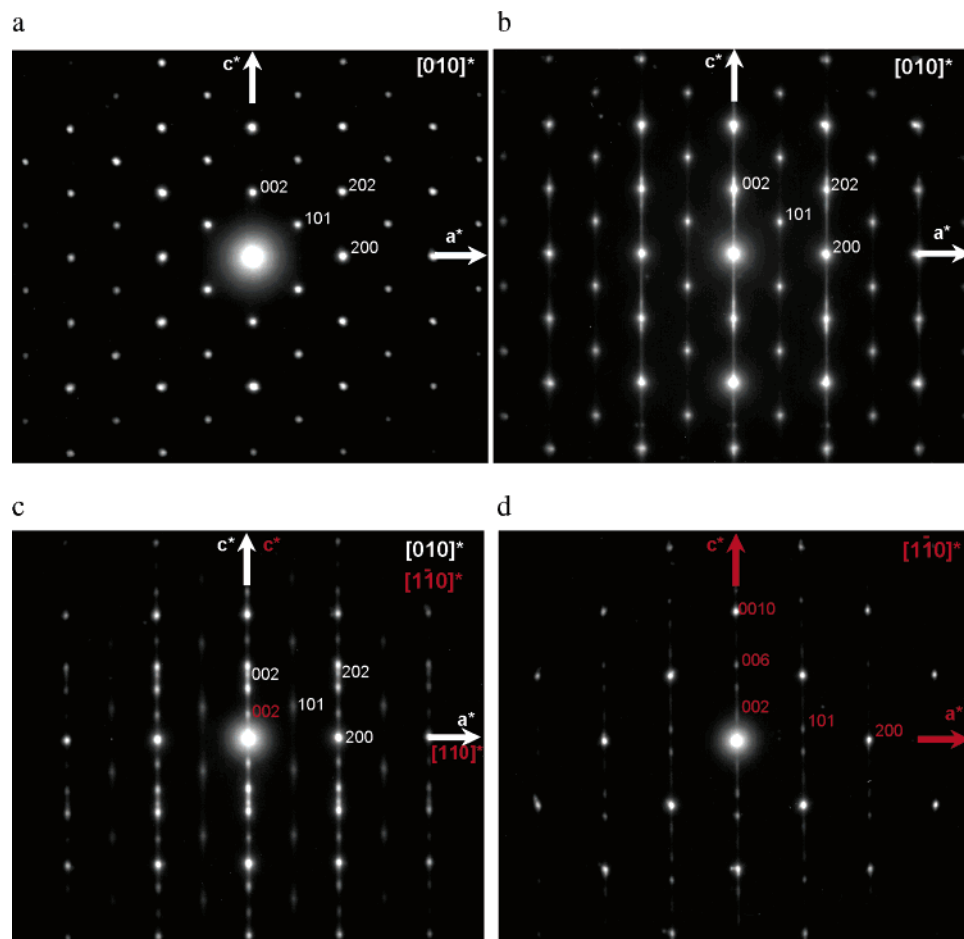
Figure 5. Selected area electron diffractograms for $Sr_2MgMoO_{6-\delta}$ sample IV reduced at 1200 °C. White indices refer to the unit cell of the $Sr_2MgMoO_{6-\delta}$ perovskite phase and red to the RP $n = 2$ phases, showing: (a) [010] projection of $Sr_2MgMoO_{6-\delta}$ perovskite alone; (b) [010] projection of $Sr_2MgMoO_{6-\delta}$ with prominent streaking along (001); (c) [010] projection of $Sr_2MgMoO_{6-\delta}$ intergrown with the [1̄10] projections of an RP $n = 2$ phase. Prominent streaking along (001) in both phases is obvious; (d) [1̄10] projection of an RP $n = 2$ phase, with streaking along (001).
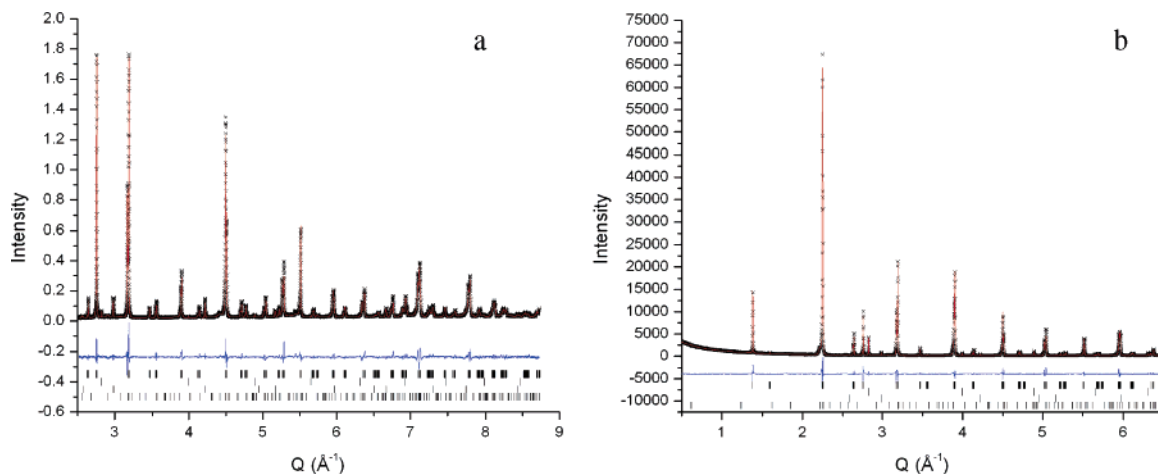
Figure 6. Rietveld refinement plots of sample III of $Sr_2MgMoO_{6-\delta}$ reduced at 1200 °C: (a) backscattering bank neutron diffraction data from HRPD and (b) powder X-ray diffraction data, represented as in Figure 3a. The tick marks show the Bragg peaks for, from top to bottom, $Sr_2MgMoO_{6-\delta}$, Mo, MgO, and the $n = 2$ RP phase $Sr_3(Mo_{(1-x)}Mg_x)_2O_{7-\delta}$ ($x = 0.215(9)$).

the refined phase fractions. The overall Sr:Mo:Mg ratios from the X-ray and neutron refinements were 1:0.57:0.53 and 1:0.54:0.52, respectively, close to the theoretical values of 1 :0.5 :0.5.

Discussion

Figure 7 shows views down the principal axis of the perovskite subcell for Sr_2MgMoO_6. Table 4 summarizes the octahedral cation bond lengths for all three samples as well as the cation bond valence sums[15] and octahedral distortion parameter ($\sum(r - r_{mean})^2$). It can be clearly seen that there is an obvious c^- tilt with little or no tilt about the other axes. Thus for the tilt system $a^0a^0c^-$, we would expect that the structure would adopt the tetragonal space group $I4/m$[16,17]

---

(15) Brown, I. D. *Acta Crystallogr., Sect. B* **1977**, *33*, 1305−1310.
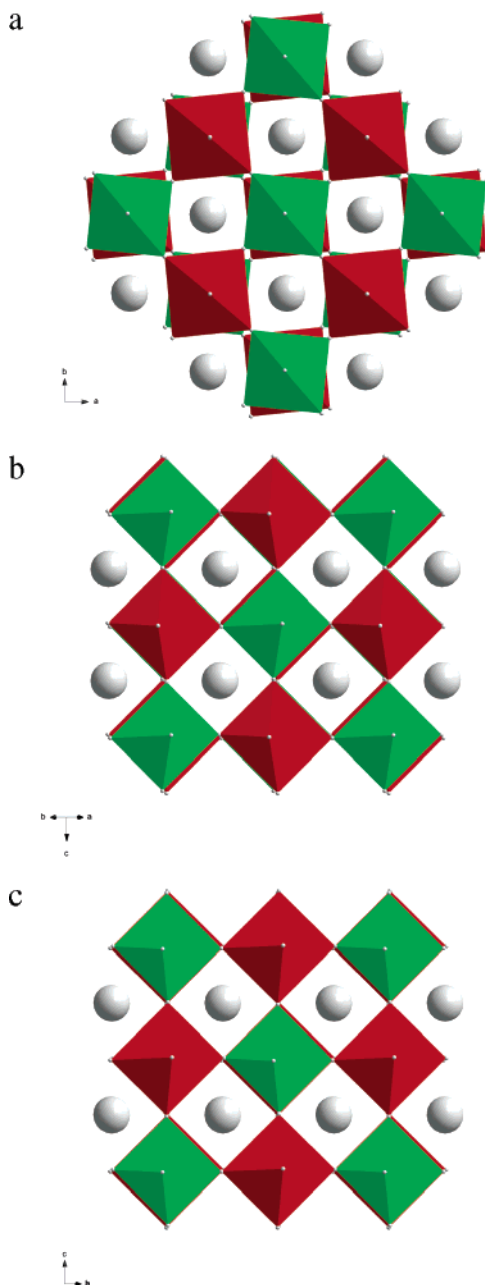
a

b

c

Figure 7. Refined structure of Sr_2MgMoO_6 (sample I) obtained from the HRPD data viewed along (a) [001], (b) [110], and (c) [1$\bar{1}$0]. Grey spheres are Sr, red octahedra are Mg-centered, and green octahedra are Mo-centered.

Table 4. Refined Bond Lengths, Calculated Bond Valence Sums,[15] and Octahedral Distortion ($\sum(r - r_{mean})^2$) at the Octahedral Sites of $Sr_2MgMoO_{6-\delta}$ (refined oxygen deficiency is given in the final row), on the Basis of Refinements against the Neutron Data

bond (Å)	I	II	III
Mo1−O1 × 2	1.9403(18)	1.9602(28)	1.953(4)
Mo1−O2 × 2	1.9335(19)	1.9475(10)	1.9662(23)
Mo1−O2b × 2	1.9376(20)	1.9424(9)	1.8866(27)
Mg2−O1 × 2	2.0221(17)	2.0059(28)	2.010(4)
Mg2−O2 × 2	2.0305(18)	2.0062(10)	2.0008(23)
Mg2−O2b × 2	2.0147(20)	2.0260(8)	2.0639(27)
Mo BVS	5.53(4)	5.34(4)	5.58(8)
Mg BVS	2.46(2)	2.53(2)	2.35(3)
Sr BVS	2.06(2)	2.05(2)	2.04(2)
($\sum(r - r_{mean})^2$) Mo−O	2.41×10^{-5}	0.000187	0.004583
($\sum(r - r_{mean})^2$) Mg−O	1.25×10^{-4}	0.000392	0.00299
δ	0.0	0.014(2)	0.046(10)

in the absence of any octahedral distortions. Using the program SPUDS[17] (Table 5), it is possible to estimate the

Table 5. Predicted Tilt Systems for 1:1 Ordered Sr_2MgMoO_6 in the Absence of Octahedral Distortions

tilt system	space group (undistorted octahedral)	global instability index (valence units)[17]
$a^+a^+a^+$	$Pn\bar{3}$	0.04236
$a^-b^+a^-$	$P2_1/n$	0.00030
$a^-a^-a^-$	$R\bar{3}$	0.00009
$a^0b^-b^-$	$I2/m$	0.00685
$a^0a^0c^+$	$P4/mnc$	0.02075
$a^0a^0c^-$	$I4/m$	0.02075
$a^0a^0a^0$	$Fm\bar{3}m$	0.13952

relative stability of various tilt systems. It can be seen from Table 5 that one might expect either the tilt system $a^-b^+a^-$ ($P2_1/n$) or $a^-a^-a^-$ ($R\bar{3}$). However, Sr_2MgMoO_6 adopts the tilt system $a^0a^0c^-$,with octahedral distortions reducing the tetragonal tilt-based symmetry to triclinic. The underlying tilt system is consistent with the I4/m structure of the Sr-based rock-salt ordered double perovskite Sr_2FeMoO_6.[18] Sr_2MgMoO_6 appears to contain more local strain than Sr_2MnMoO_6,[19] where the Mo bond valence sum is 5.77, and the mean square distortion at the Mo octahedral site is 4.27×10^{-5}. This supports the suggestion that the symmetry-lowering from I4/m is driven by octahedral distortion. In all three refined structures, the Mo appears underbonded and the Mg significantly overbonded.

Figure 8 shows the response of Sr_2MgMoO_6 to reduction. Both the unit-cell volume and the cation occupancy disorder on the octahedral site correlate well with the refined oxygen deficiency ($\delta = 0$, 0.014(2) ,and 0.046(10) with corresponding values of the octahedral disorder of 0.008(2), 0.013(1), and 0.057(1) for samples I−III, respectively). It should also be noted that it is a consistent feature of the Rietveld refinements that only one of the three oxygen sites (O2b) appears to be depleted. The mean square distortion at the octahedral Mo and Mg sites increases systematically with the amount of reduction.

It is particularly interesting to observe that disorder of the octahedral sites correlates almost quantitatively with the number of oxide anion vacancies. This could be interpreted as the avoidance of low coordination numbers for Mg, for which coordination numbers of less than 6 are rare in oxides. If we consider only antisite disorder, each swap of cation pairs (to produce Mg on a Mo site and Mo on a Mg site) produces five Mg−O−Mg linkages and five Mo−O−Mo linkages (Figure 9). The creation of the Mo−O−Mo linkages thus produces oxide anions that are coordinated purely to Mo. Removal of these anions will produce only five-coordinate Mo(V), which is well-established, removing the necessity to propose the formation of five-coordinate Mg^{2+} in an oxide. The observed correlation between oxide vacancy content and cation site order is thus chemically justifiable. However, only Mo−O2b−Mo linkages appear to be reduced according to the site occupancy refinements for samples II and III. This is consistent with the observation that the Mo−

(16) Howard, C. J.; Kennedy, B. J.; Woodward, P. M. *Acta Crystallogr., Sect. B* **2003**, *59*, 463−471.
(17) Lufaso, M. W.; Barnes, P. W.; Woodward, P. M. *Acta Crystallogr., Sect. B* **2006**, *62*, 397−410.
(18) Nakamura, S.; Oikawa, K. *J. Phys. Soc. Jpn.* **2003**, *72*, 3123−3127.
(19) Azad, A. K.; Eriksson, S.-G.; Ivanov, S. A.; Mathieu, R.; Svedlindh, P.; Eriksen, J.; Rundlof, H. *J. Alloys Compd.* **2004**, *364*, 77−82.
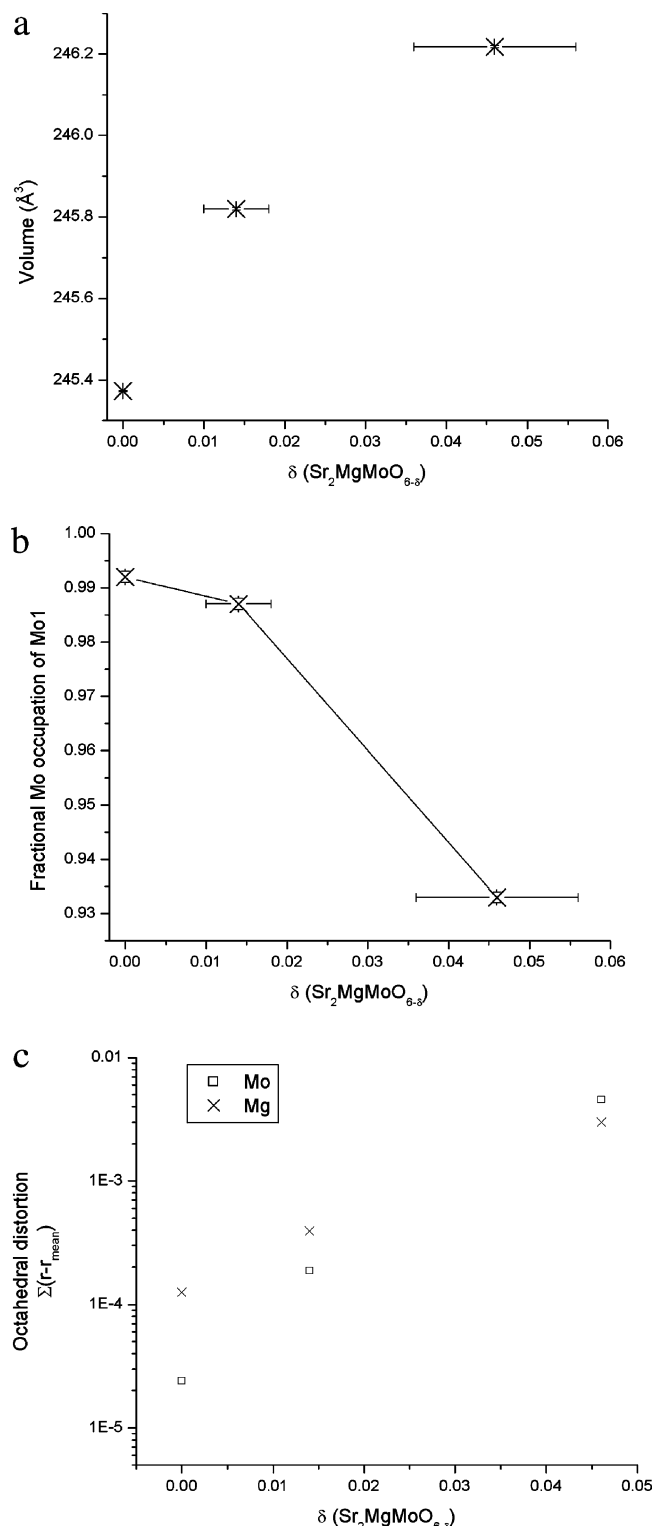
Sr₂MgMoO₆₋δ: Structure, Stability, and Cation Site Order Control

Chem. Mater., Vol. 19, No. 5, 2007 1041

a

b

c

Figure 8. Correlation of refined parameters for $Sr_2MgMoO_{6-\delta}$ with refined vacancy concentration δ: (a) unit-cell volume against refined oxygen content (sample I is assumed to be stoichiometric in oxygen); (b) fractional Mo occupancy of the Mo1 site vs refined oxygen content; (c) octahedral distortion parameter ($\Sigma(r - r_{mean})^2$).

O2b distance is the most sensitive of all the Mo–O distances to reduction (Figure 10a).

It has been argued in similar B-site ordered perovskites that apparent antisite disorder is primarily due to stacking faults at which there is a phase shift in the cation occupancies and the resulting formation of antiphase domain boundaries.[20] In the case of $A_2BB'X_6$ systems,[21] considered in terms of a

$2a_p \times 2a_p \times 2a_p$ cell, which, for $Sr_2MgMoO_{6\pm\delta}$, would represent an $F\bar{1}$ cell ($a' = a + b$, $b' = a - b$, $c' = c$), both [100] and [110] antiphase boundaries (within this F-centered cell) conserve the cation composition while generating Mo–O–Mo sites where reduction would occur along the boundary where the unfavorable cation pairs are concentrated. This is illustrate schematically in Figure 9c. Extended defects of this type would reduce the number of electrostatically unfavorable interactions per cation. Note that the aggregation of oxide vacancies upon reduction to form extended defects has been used to explain the metallic conductivity of $SrTiO_3$ even at very low degrees of reduction, as it permits a connected pathway between the reduced transition metal centers.[22]

It can also be seen in Figure 8c that the octahedral distortion of both Mg and Mo increase with extent of reduction, although Mo increases more rapidly. The reason for this can be seen in Figure 10b, where the largest change in bond lengths occurs between Mo and O2b. The enhanced sensitivity of the Mo–O2b distance to the extent of reduction correlates with the enhanced vacancy concentration refined at this site. It should be noted that the O2b sites lie along one [001] plane in the $F\bar{1}$ cell. This is consistent with the removal of oxide anions in a manner correlated with the formation of extended defects within this plane. The presence of significant amounts of such [001] antiphase boundaries is also consistent with the observed streaking in Figure 5b, in the absence of observable RP $n = 2$ type intergrowth superstructure spots discussed in the next paragraph. The compositional and electron diffraction evidence is thus consistent with the formation of extended arrays of antisite defects, which would minimize both the formation of five-coordinate Mg and unfavorable local cation pairings due to isolated antisite disorder while creating extended electronic conduction paths through the sample.

Reduction of Sr_2MgMoO_6 at high temperature produces a change in the observed phase assemblage driven by the formation of an $n = 2$ Ruddlesden–Popper phase. Figure 11 shows the derived structural model of $Sr_3(Mo_{(1-x)}Mg_x)_2O_{7-\delta}$ ($x = 0.215(9)$, $\delta = 0.49(3)$). The exact nature of this phase is unclear, in the absence of the observation of distinct grains of the segregated RP phase by EDX, as is the significant broadening of the peaks for both perovskite and RP Sr–Mg–Mo–O phases in sample III. (The refined Stephens anisotropic strain parameters for the perovskite phase are 5–10 times greater in sample III as compared to sample I.) The complex streaking in the electron diffraction patterns recorded from sample III (Figure 5) indicate that the true nature of the phase assemblage is more complex. It is thus likely that the secondary RP phase is significantly intergrown with the perovskite phase given the significant refined phase fraction, though the observation of distinct Bragg reflections from the $n = 2$ RP structure in Figure 5d indicates that there are some coherent domains. The X-ray refinements show

(20) Ting, V.; Liu, Y.; Noren, L.; Withers, R. L.; Goossens, D. J.; James, M.; Ferraris, C. *J. Solid State Chem.* **2004**, *177*, 4428–4442.
(21) Woodward, P.; Hoffmann, R. D.; Sleight, A. W. *J. Mater. Res.* **1994**, *9*, 2118–2127.
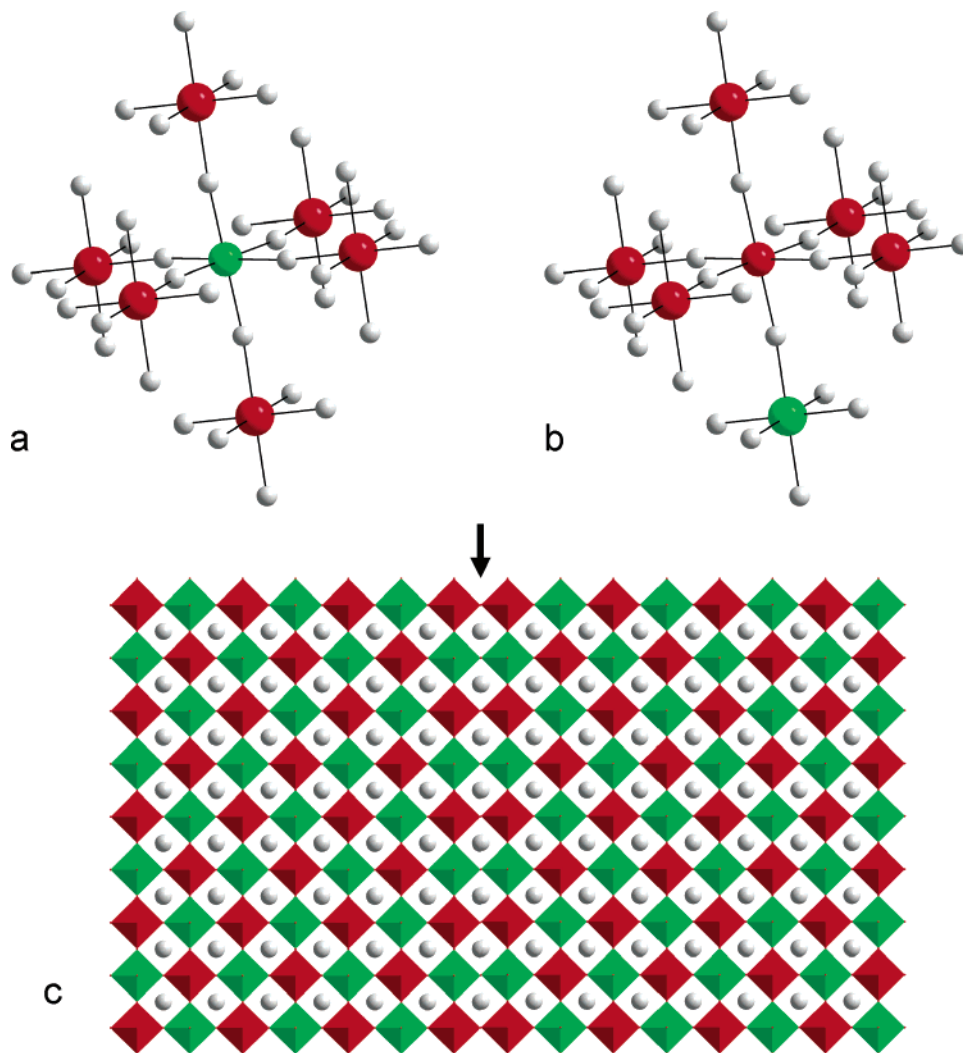(22) Szot, K.; Speier, W.; Carius, R.; Zastrow, U.; Beyer, W. *Phys. Rev. Lett.* **2002**, *88*, 075508.

Figure 9. Schematic illustration of models for antisite disorder in $Sr_2MgMoO_{6\pm\delta}$: (a) Molybdenum (green) surrounded by six next-nearest-neighbor magnesium (red) in a perfectly B-site ordered material; oxygens are white and strontium cations are omitted for clarity. (b) Situation after a single molybdenum–magnesium B-site swap. There are now five unfavorable next-nearest-neighbor interactions per cation. (c) Schematic representation of a $[100]_{perov}$ antiphase extended defect indicated with an arrow; red octahedra are magnesium centered and green molybdenum centered. Note that, in this case, only one unfavorable next nearest neighbor interaction per cation is introduced.
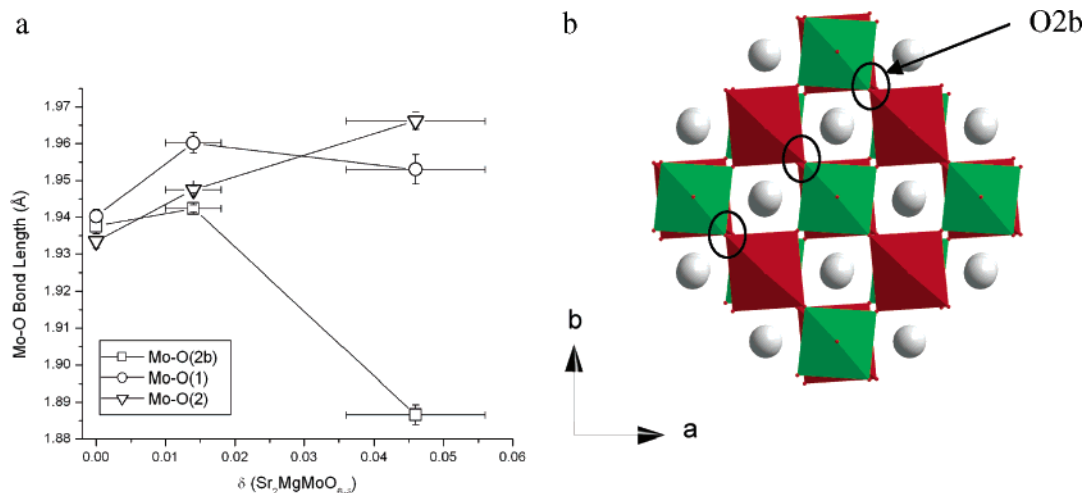
Figure 10. (a) Three crystallographically distinct Mo−O distances in $Sr_2MgMoO_{6-\delta}$ versus refined oxygen stoichiometry. (b) Sructure of $Sr_2MgMoO_{6-\delta}$ viewed along [001] showing the location of O2b, which lies in [100] planes within the perovskite subcell.

that these intergrowths are Mo-rich with a B-site composition of $Mo_{0.785(9)}Mg_{0.215(9)}$. Importantly, this B-site composition combined with the refined fraction for all four phases in the complex assemblage is consistent with the overall cation composition Sr_2MgMo. The neutron data show that these Ruddlesden−Popper intergrowths are significantly reduced and accommodate reduction of molybdenum to a level beyond that possible in the perovskite phase: this can be
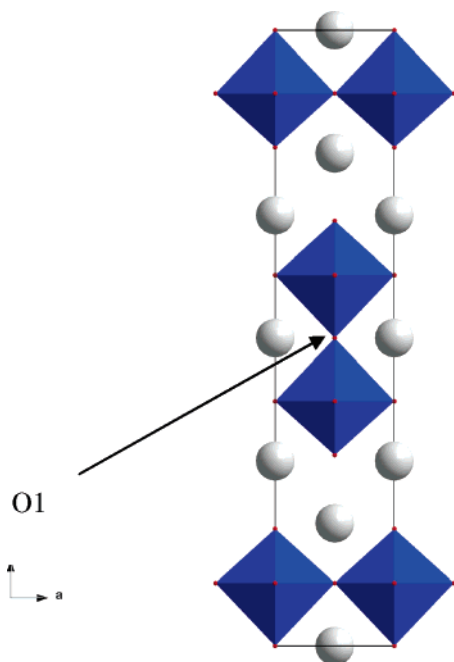
Figure 11. Refined structure of the $n = 2$ Ruddlesden−Popper phase $Sr_3(Mo_{1-x}Mg_x)_2O_{7-\delta}$ ($x = 0.215(9)$, $\delta = 0.49(3)$; sample III) obtained from the HRPD data viewed along [010]; O1 is labeled to show the location of the oxygen vacancies (bond lengths: Mo1−O1, $1 \times 2.163(10)$ Å; Mo1−O2, $1 \times 1.729(15)$ Å; Mo1−O3, $4 \times 1.9775(4)$ Å).

attributed to the enhanced Mo content, which permits the removal of oxygen without the formation of five coordinate Mg^{2+}. The refined $Sr_3(Mo_{0.785(9)}Mg_{0.215(9)})_2O_{6.51(3)}$ composition gives a molybdenum oxidation state close to Mo^{IV}, which is chemically sensible given the existence of $Sr_3Mo_2O_7$ and the Zn^{2+}-containing phase $Sr_3Mo_{1.5}Zn_{0.5}O_{6.75}$.[23] This reduced character and oxygen deficiency lead to the expectation that the $n = 2$ Ruddlesden−Popper phase or intergrowths would have significant electronic and ionic conductivities.

Conclusions

We have shown that Sr_2MgMoO_6 adopts an $I\bar{1}$ structure derived from an $a^0a^0c^-$ tilt system related to that of Sr_2FeMoO_6 via distortion of the Mg- and Mo-centered octahedra. Reduction of the perovskite Sr_2MgMoO_6 is possible only to a limited extent despite the stability of lower Mo oxidation states than +VI, which is attributed to the difficulty of forming five coordinate Mg^{2+} in the perovskite structure. The extent of reduction that is possible within the

perovskite is correlated with antisite disorder of the Mo and Mg cations, which permits the removal of oxide anions while only reducing the coordination number of Mo. The assimilation of point antisite defects into extended structures analogous to antiphase domain boundaries would minimize unfavorable electrostatic interactions arising from antisite defect formation and permit the correlated removal of oxide anions. Upon further reduction at temperatures >900 °C $Sr_2MgMoO_{6\pm\delta}$ assumes a higher O vacancy content but begins to decompose into a reduced material modeled as an $n = 2$ RP phase with a significantly higher Mo:Mg ratio, MgO, and Mo and a lower Mo oxidation state. One plausible model of the reduction would thus involve initial reduction associated with extended antisite defects followed by decomposition at these defects by excision of BO_6 octahedral layers neighboring the defect, yielding intergrowth of an RP = 2 material in a perovskite matrix.

The reactivity of $Sr_2MgMoO_6\pm_\delta$ suggests other approaches to the formation of fuel cell anodes in this phase field. Molybdenum metal or, under some of the feed conditions tested, molybdenum carbide[24] or sulfide[25] is likely to be catalytically active as is, potentially, the intergrowth of $Sr_3(Mo_{(1-x)}Mg_x)_2O_{7-\delta}$. To understand the observed behavior of $Sr_2MgMoO_{6\pm\delta}$ cathodes further, we require detailed studies of the phase assemblies in working electrodes to understand the exact roles of the different potential components. We are currently investigating the synthesis of $Sr_3(Mo_{(1-x)}Mg_x)_2O_{7-\delta}$ and related Ruddlesden−Popper phases in order to study their electronic and catalytic properties.

Supporting Information Available: Powder XRD for samples III and IV are available (PDF) together with crystallographic information files for all the refinements (CIF). This material is available free of charge via the Internet at http://pubs.acs.org.

CM0624116

(23) Steiner, U.; Reichelt, W.; Schmidt, M.; Schnelle, W. *Z. Anorg. Allg. Chem.* **2004**, *630*, 649−654.

(24) Claridge, J. B.; York, A. P. E.; Brungs, A. J.; Marquez-Alvarez, C.; Sloan, J.; Tsang, S. C.; Green, M. L. H. *J. Catal.* **1998**, *180*, 85−100.
(25) Osaki, T.; Horiuchi, T.; Suzuki, K.; Mori, T. *Catal. Lett.* **1995**, *35*, 39−43.